Design of electric motor for e-bike application

Chiara Contò
University of Padova
Dep. of Industrial Engineering
Padova, Italy
chiara.conto@phd.unipd.it

Nicola Bianchi
University of Padova
Dep. of Industrial Engineering
Padova, Italy
nicola.bianchi@unipd.it

***Abstract*—This paper focuses on the design of an electric motor for e-bike application. It aims to provide guidelines for choosing and designing electric motors for e-bikes, with a focus on permanent magnet synchronous motors. The analysis combines a preliminary analytical model and finite element analysis simulation to test different motor geometries and verify results with experimental data from commercial motors. The goal is to provide a detailed general procedure for the design of e-bike electric motors and contribute to the development of more eco-friendly mobility.**

***Index Terms*—Electric bicycle, Electric motor design, Permanent magnet motors, Interior permanent magnet motors**

I. Introduction

Electric bicycles, or e-bikes [1], have gained popularity in recent years due to their environmental benefits and convenience. The e-bike market is expected to grow at a rate of 10% per year, reaching a market size of nearly USD 48.5 billion by 2028 [2]. Light Electric Vehicle (EV) mobility requires high-performance electrical motors that exhibit high torque at low speed, and constant output characteristics over a wide range. Permanent Magnet Synchronous Motors (PMSMs) are the best choice for traction motors [3]. In regards to electric motor typology, brushless DC electric motors are the subject of much of the literature, including studies such as [4]–[8].

Although Permanent Magnet (PM) motors are actually the best solution for traction application, the high cost and decreasing availability of magnetic materials, particularly rare-earth PMs, motivate the search for alternative solutions. Studies of the design of innovative motors for e-bike application can be found in the literature. For example, [9] presents an innovative design for an in-hub outer rotor PM-assisted synchronous reluctance motor. The synchronous reluctance machine capability is enhanced by adding PMs into rotor barriers. Consequently, the torque density is enhanced of 28%, while simultaneously reducing cogging torque and torque ripple by 50% and 8%, respectively. Furthermore, this design reduces the usage of PMs and corresponding cost by 40% compared to a commercial brushless DC motor.

This study is partially supported by Department of Industrial Engineering, University of Padova, by means of the project SID BIRD224007 and partially carried out within the NEST - Network 4 Energy Sustainable Transition (D.D. 1243 02/08/2022, PE00000021) and the project is funded Project funded under the National Recovery and Resilience Plan (NRRP), Mission 4 Component 2 Investment 1.3 - Call for tender No. 1561 of 11.10.2022 of Ministero dell'Università e della Ricerca (MUR), funded by the European Union - NextGenerationEU.

Studies have also examined e-bike electric motors with switched reluctance technology, such as [10] and [11]. These studies explore the in-wheel external rotor structure and the optimization of a switched reluctance motor design, respectively, with the goal of achieving performance parameters and dimensional constraints of a commercial PM e-bike motor.

While synchronous reluctance motors can be considered as an alternative to PM synchronous motors in e-bike applications due to their low cost and robust construction, they suffer from high torque ripple and acoustic noise generation. Therefore, this work focuses on the PM synchronous motor topology, which overcomes some limitations of reluctance machines and is increasingly popular in light EV applications. Notably, literature on PM synchronous motors for electric bicycles is limited, despite the fact that such machines satisfy the performance requirements of the e-bike application. PM machines exhibit high torque density, particularly at low speeds, which is a current trend in the development of high-performance motors for e-bikes. In addition, considering e-bike application, fractional-slot concentrated windings [12], [13], which have a non-integer number of slots per pole per phase, are commonly employed. These windings have several advantages, such as being suitable for high-pole machines [14] and having reduced end-winding lengths, which leads to lower copper weight and Joule losses. However, they can also have a high torque ripple, a low winding factors or magneto motive force sub-harmonics which cause additional rotor losses and torque ripple.

The purpose of this study is to provide guidelines for an electric motor design by analysing different motor geometries and their performance. The novelty consists in finding design limits of a PMSM for e-bike application, but also defining a region of enhanced performance and identify the parameters which allow such improvement. Once the analytical model is verified, various motor geometries are tested using preliminary experimental results from commercial motors. All feasible geometries are analysed through two-dimensional magneto-static Finite Element (FE) analysis simulation. The target values are evaluated and analysed producing maps to represent their dependence on the model variables, avoiding typical closed formulas.

The paper is outlined as follows. In Section II some preliminary simulations on a commercial Interior Permanent Magnet (IPM) motor are carried out. The nominal and overload operation of the motor are defined. Section III presents a simple

TABLE I
IPM SPOKE MOTOR EXPERIMENTAL TEST RESULTS.

Current (A peak)	Current density (A rms/mm^2)	Torque (N m)	Power (W peak)	Temperature (°C)
8	3.6	0.77	240	47
14	6.3	1.46	420	94
20	9	2.06	600	100

analytic model for the Surface-mounted Permanent Magnet (SPM) machine. Its design equations are presented and a brief description of capabilities evaluation is given. FE simulation results are exposed in Section IV. Similarly, the IPM motor configuration is analysed. Its analytical model is described in Section V, while FE simulation results are exposed in Section VI. The final map of performance capabilities includes the tested motor configuration. An alternative optimized design solution is presented.

II. Preliminary Test on Commercial Motors

As defined by EU regulations, the electric assistance is limited to a maximum speed of 25 km/h and a maximum power of 250 W. Even though the continuous power of the motor is limited, the motor drive is designed to exhibit temporary power that is much higher. The battery is usually a low-voltage lithium-ion with a typical DC bus voltage of 36 V, although 48 V-batteries are becoming popular.

Fig. 1 shows the experimental test results for a commercial motor with the 12 slots/10 poles configuration and an Interior Permanent Magnet (IPM) rotor geometry. A preliminary thermal test on the stator winding (Fig. 1a) is carried out to identify the rated current. It underlines that the 14 A peak current is the nominal value, since the steady-state temperature reached (94 °C) can be sustained during nominal operation. Such current corresponds to a RMS current density of 6.3 A/mm^2. Joule losses computed for this measure are equal to 34.5 W, iron losses are 9.4 W, thus total losses amount to 43.9 W.

Two additional measures with current amplitude 8 A peak and 20 A peak are presented. The steady-state temperatures reached are 42 °C and 120 °C, respectively. The 20 A peak can be sustained for a maximum time of 3 min, when the temperature reaches 100 °C.

For each peak current supplied, torque (Fig. 1b) and power (Fig. 1c) are represented for different speeds, considering a DC bus voltage of 36 V. When the 8 A peak current is supplied the torque delivered 0.8 N m, while with the current 20 A peak it is 2.1 N m. The rated speed is about 2800 rpm. The output power is 240 W when the 8 A peak current is supplied, 420 W when the 14 A peak current is supplied and 600 W when the 20 A peak current is supplied.

III. Analytical Model of the SPM Motor

A. Motor configuration and fixed parameters

The SPM motor is tested with a typical 12 slots/10 poles fractional-slot configuration. TABLE II summarizes the main motor parameters adopted in the analysis, fixed by design rules

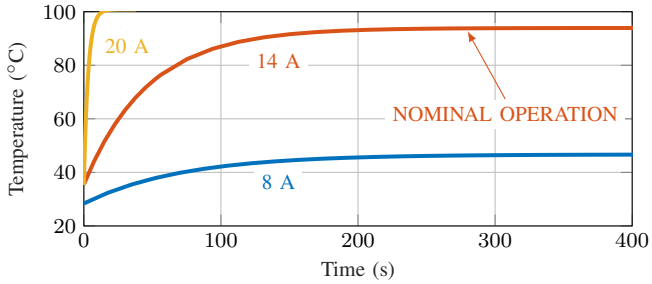

(a) Temperature vs time.

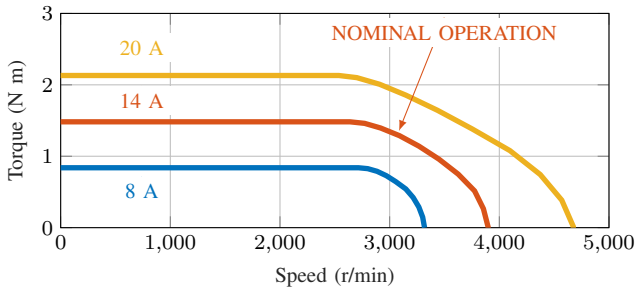

(b) Torque vs speed.

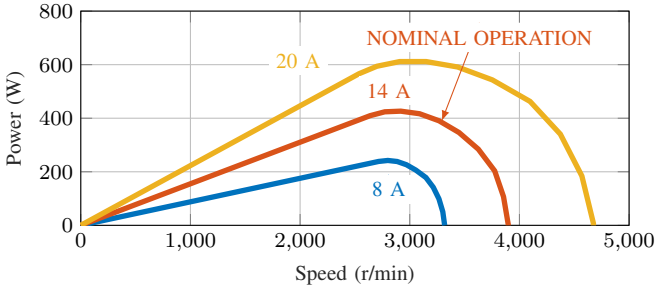

(c) Power vs speed.

Fig. 1. Experimental tests on a 12 slots/10 poles commercial motor.

TABLE II
MOTOR CONFIGURATION PARAMETERS AND GEOMETRY.

Parameter	Symbol	Value	Unit
Number of slots	Q	12	-
Number of poles	$2p$	10	-
frequency	f	250	Hz
External diameter	D_e	80	mm
Shaft diameter	D_{sh}	10	mm
Stack length	L_{stk}	25	mm
Air gap length	g	0.5	mm

and state-of-the-art data. TABLE III specifies material properties. The frequency is assumed to be the maximum power frequency, which leads to a speed $n = 60 \cdot f/p = 3000$ rpm.

The analytical model includes two main variable parameters: the stator inner diameter D and the current density J_s. Stator diameter minimum and maximum values are 15 mm and 65 mm, respectively. Current density minimum and maximum values are 6 A/mm^2 and 10 A/ mm^2.

TABLE III
PM PROPERTIES AND SATURATION LIMITS.

Parameter	Symbol	Value	Unit
Remaining flux	B_{rem}	1.12	T
Relative permeability	μ_{rec}	1.06	-
Max value in tooth	B_t	1.8	T
Max value in back-iron	B_{bi}	1.6	T

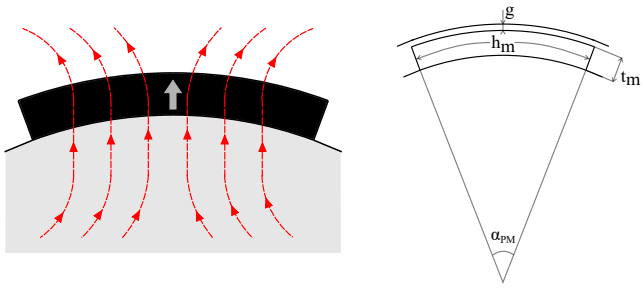

Fig. 2. SPM motor PM flux lines.

B. Motor analytic model and design

The analytical model aims at exploring different design solutions to find which motor geometry maximizes the performance. The models are generated by the combination of the external diameter D and the current density J_s values. The main equation is the analytical expression of the air gap flux density for the SPM motor. In can be computed from fundamental electro-magnetic equations, considering flux lines represented on the left part of Fig. 2 and geometric parameters of the right part of the same picture. PM dimensions are thickness t_m and length h_m, that depends on the angle spanned by the PM itself α_{PM}. The equations are the following:

$$\begin{cases} B_m \cdot h_m \cdot L_{stk} = B_g \cdot \frac{\pi \cdot D}{2p} \cdot L_{stk} \\ H_m \cdot t_m + H_g \cdot g = 0 \\ B_g = \mu_0 \cdot H_g \\ B_m = B_{rem} + \mu_0 \cdot \mu_{rec} \cdot H_m \end{cases} \tag{1}$$

where, the first is the Gauss's law applied to the flux generated by the PM that flows through the air gap, the second is Ampere's law along a line which follows the trajectory of red curves of Fig. 2 and the other two are constitutive equations. Solving the system, the air gap flux density can be expressed as a function of main material and geometric parameters:

$$B_g = \frac{B_{rem}}{\frac{\pi \cdot D}{2p} \cdot \frac{1}{h_m} + \mu_{rec} \cdot \frac{g}{t_m}} \tag{2}$$

As expected, the flux-density in the air gap increases as the PM dimensions increase. The PM thickness selected is $t_m = 5$ mm, while the PM length is computed considering that the PM spans a high percentage of the pole angle. The PM angle considered is $\alpha_{PM} = 0.9 \cdot \alpha_p = 0.9 \cdot \pi/p$, thus the PM length is $h_m = (D - g)/2 \cdot \alpha_{PM} = 6.8$ mm.

Finally, the air gap flux density is obtained from equation (2). Then, the air gap flux is $\Phi_g = B_g \cdot D \cdot L_{stk}/p$. The stator back-iron height, is designed in order to avoid saturation. From the relationship between the pole flux Φ_g and the back-iron flux Φ_{bi}:

$$\Phi_g = 2 \cdot \Phi_{bi} \quad \rightarrow \quad B_g \cdot \frac{D \cdot L_{stk}}{p} = 2 \cdot B_{bi} \cdot h_{bi} \cdot L_{stk} \tag{3}$$

where B_{bi} is imposed as reported in TABLE III, the back-iron height can be computed.

Other the motor geometric parameters can be computed by means of geometric equations and fundamental electric motor design rules. In particular, the slot height is $h_s = (D_e - D)/2 - h_{bi}$ and the tooth width has the dimension required to avoid saturation: $w_t = B_g/B_t \cdot \pi \cdot D/Q$.

C. Performance evaluation

Through an approximate computation of the slot area S_{slot} and the current density variable J_s, the load current is $I_{slot} = \sqrt{2} \cdot J_s \cdot k_{fill} \cdot S_{slot}$. The electric load K_s is computed as $K_s = I_{slot} \cdot k_w \cdot Q/(\pi D)$. The torque is:

$$\tau = K_s \cdot B_g \cdot \pi/4 \cdot D^2 \cdot L_{stk} \tag{4}$$

Stator Joule losses are computed as:

$$P_{J,s} = J^2 \cdot V_{Cu,s} \cdot \rho_{Cu,120^\circ} \tag{5}$$

where $\rho_{Cu,120^\circ}$ is the copper resistivity at the working temperature and $V_{Cu,s}$ is the volume of copper material in the stator.

Iron losses are computed by Steinmetz formulation, considering both hysteresis and eddy currents effects. Specific iron losses are computed considering the maximum flux density reached $\hat{B}$ and the specific frequency compared to the reference flux density $B^*_{fe} = 1.5$ T and frequency $f^* = 50$ Hz, respectively. Hysteresis accounts for 70 % of iron losses (coefficient $k_h = 0.7$), while eddy currents for 30 % of iron losses (coefficient $k_{ec} = 0.3$). Thus, specific iron losses are calculated as:

$$p_s = p^*_{s,fe} \cdot \left(\frac{\hat{B}}{B^*_{fe}}\right)^2 \cdot \left[k_h \cdot \left(\frac{f}{f^*}\right) + k_{ec} \cdot \left(\frac{f}{f^*}\right)^2\right] \tag{6}$$

Considering iron weight G and an increase coefficient due to manufacturing k_m, iron losses are $P_{fe} = k_m \cdot p_s \cdot G$. Two different regions are considered: the back-iron, which causes iron losses $P_{fe,bi}$, and the teeth, which cause the iron losses $P_{fe,t}$. Specific losses are computed by (6) considering the maximum flux density value in the specific region, i. e. $\hat{B}_{bi}$ in the back-iron, $\hat{B}_t$ in teeth. Iron losses in teeth are computed considering an increase coefficient $k_{m,t} = 2$, while back-iron losses include an increase coefficient $k_{m,t} = 1.5$.

Finally, total losses are $P_{loss} = P_{J,s} + P_{fe,bi} + P_{fe,t}$. As the frequency is considered constant, the mechanical speed ω_m and the torque delivered allow to esteem the output power as $P_{out} = \tau \cdot \omega_m = \tau \cdot 2\pi f/p$. The motor efficiency can be calculated.

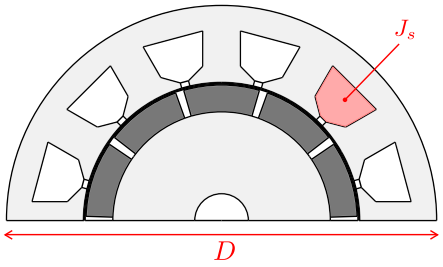

Fig. 3. SPM motor model.

IV. Results for the SPM motor

This Section focuses on the SPM motor, both analytical and finite simulation results. Magneto-static simulations are carried out through 2-D finite element analysis by means of $femm$ 4.2 software [15]. The SPM motor model considered for simulations is represented in Fig. 3, where its variable parameters are underlined. In particular, D varies from a minimum value of 15 mm and a maximum of 65 mm. In combination with the variation of the diameter, the current density varies from a minimum of 6 $\mathrm{A/mm^2}$ and a maximum of 10 $\mathrm{A/mm^2}$.

Therefore, the SPM motor performance is evaluated for each diameter and current density combination. The torque is computed both analytically and by means of FE simulations. Fig. 4 shows that analytical results are quite similar to FE simulation results. In both computations an optimal stator internal diameter can be identified, since a specific torque can be delivered with the minimum current density. In the analytical procedure the optimal diameter results 30 mm, while through FE simulations it is 36.4 mm.

V. Analytical model of the IPM motor

A. Motor configuration and fixed parameters

The IPM motor studied has a spoke-type PM rotor. As carried out for the SPM motor, the IPM configuration is the 12 slots/10 poles fractional-slot configuration, with main parameters exposed in TABLE II. Material properties are presented in TABLE III as well. The speed considered is still the 3000 rpm, i. e. a frequency of 250 Hz.

Since the PMs are arranged radially (a spoke disposition) they produce a tangential flux and the magnetizing flux produced by one PM is added to that produced by the adjacent PM, resulting in the so-called concentrated flux configuration. This geometry allows for a high number of PMs, and consequently a high torque density, which is highly desired in electric bicycle applications. The IPM-spoke machine is characterized by the same parameters defined in Section III-A, except for the current density and the PM dimensions. The current density is fixed to a nominal value of 7 $\mathrm{A/mm^2}$, that is a typical value to avoid high temperatures. PM thickness t_m is constant equal to 5 mm, while its height h_m is a variable parameter.

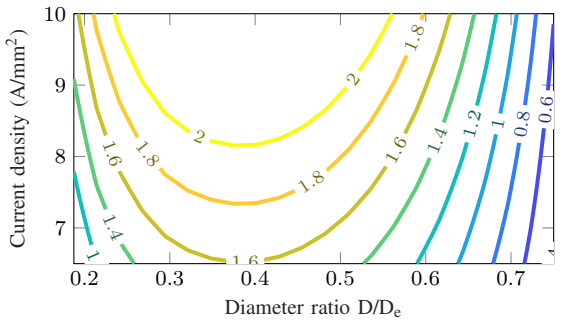

(a) Analytic computation.

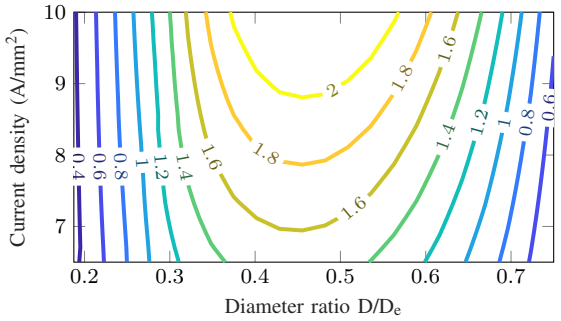

(b) FE simulation.

Fig. 4. Torque map varying D and J_S.

B. Motor analytic model and design

The analytical calculation of the flux density of an IPM motor geometry is more complex than the SPM motor. It can be computed from fundamental electro-magnetic equations, considering the model of Fig. 5a. As observed in Fig. 5b, the spoke PM arrangement includes two air gaps above and below the PM, which cause leakage flux. Since the most of leakage flux is caused by the inferior gap, the superior gap effect is neglected. The inferior gap dimensions are the height h_{inf} and the width w_{inf}. Electro-magnetic equations that describes the IPM model are the following:

$$\begin{cases} H_m \cdot t_m + H_g \cdot 2g = 0 \\ H_m \cdot t_m + H_{inf} \cdot w_{inf} = 0 \\ B_m \cdot h_m \cdot L_{stk} = B_g \cdot \frac{\pi \cdot D}{4p} \cdot L_{stk} + B_{inf} \cdot h_{inf} \cdot L_{stk} \\ B_g = \mu_0 \cdot H_g \\ B_{inf} = \mu_0 \cdot H_{inf} \\ B_m = B_{rem} + \mu_0 \cdot \mu_{rec} \cdot H_m \end{cases} \tag{7}$$

where, the first Ampere's law along a line which crosses goes through the PM and crosses the air gap, the second is Ampere's law along the red line of Fig. 5c, the third is Gauss's law applied to the flux generated by the PM that flows through the air gap, and the last three are constitutive equations. Solving the system, the air gap flux density can be expressed as a function of main material and geometric parameters:

$$B_g = \frac{B_{rem}}{\frac{\pi \cdot D}{4p} \cdot \frac{1}{h_m} + 2g \cdot \left(\frac{\mu_{rec}}{t_m} + \frac{h_{inf}}{w_{inf}} \cdot \frac{1}{h_m} \right)} \tag{8}$$

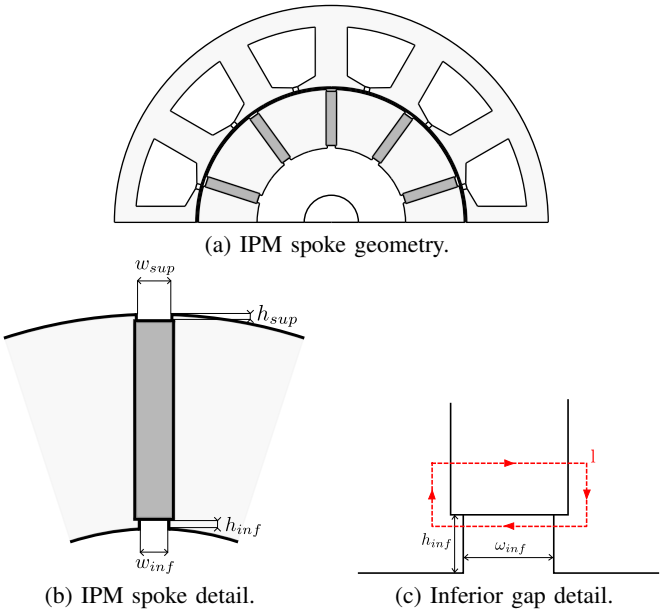

(a) IPM spoke geometry.

(b) IPM spoke detail.

(c) Inferior gap detail.

Fig. 5. IPM spoke motor model.

The air gap flux density has an quasi-squared waveform, since the flux density is equal to the peak only along the surface of the air gap in front of the magnet, while it drops between two opposite poles. After calculating the flux density of the air gap, all geometric parameters can also be computed. The procedure followed is explained at the end of the section III-B.

VI. Results for the IPM motor

As already introduced in Section V-A, the IPM motor design is explored considering a fixed current density J_s of 7 $\mathrm{A/mm^2}$ and varying PM height h_m and stator internal diameter D. The diameter varies from 45 mm to 65 mm. PM height varies in the range 10 mm − 20 mm. Since each geometry analysed results from the direct combination of h_m and D, the machine feasibility must be verified. In particular, the PM height has to fit the rotor back-iron space:

$$D/2 - D_{sh}/2 - g - (h_m + h_{sup} + h_{inf}) \geq 0 \qquad (9)$$

A. No-load flux density

First of all the air gap flux density computed analytically is compared to the one from FE simulations, considering a zero current supplied. Fig. 6 shows the comparison of the flux density waveform computed analytically and by means of fem analysis for one of the geometries tested. Its parameters are $h_m = 7$ mm and $D = 45$ mm. Two different fem simulations are carried out: one with linearity of the iron material and without stator slots (called *fem linear*), another with non-linear material properties and with stator slots effect (called *fem non linear*). The non linear fem result is similar to the analytical result, but with the slot effect, i. e. a flux density fall in correspondence to the slot opening interface.

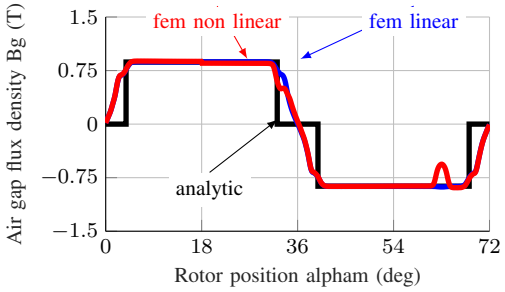

Fig. 6. Air gap flux density waveform,analytic and FE comparison.

The maximum constant value of the flux density waveform equals to 0.869 T for the analytic computation, 0.872 T for the linear FE simulation and 0.866 T for the non linear FE simulation. Comparing the first harmonic amplitude, the analytic results 1.05 T, from linear FE simulation is 1.08 T while from the non linear FE simulation it results 1.07 T.

B. Design exploration

Fig. 7 shows some results of the analytical and FE analysis of several machine geometries, resulting from the combination of all D and h_m values. Fig. 7 shows the analytic and femm linear flux density variation along the $(D_i/D_e, h_m)$ plane. The analytical prediction fits perfectly the FE results even varying the geometric parameters. Such result validates the analytical model developed.

Fig. 7b shows the torque map with respect to the diameter ratio (stator diameter versus external diameter D/D_e) and the PM length. The analytical torque is quite close to FE torque, especially for diameter ratio higher than 0.65. For a specific PM length, the torque increases as the ratio D/D_e decreases. It is worth noting that, fixing a desired value for the torque, the PM length (thus the magnetic material volume) can be minimized selecting the optimal diameter ratio.

Fig. 7c shows the comparison between analytic and FE Joule losses with respect to the diameter ratio and the PM length. They are very close to each other and they vary a lot with the diameter and slightly with the PM height. Iron losses are not considered for the comparison since they are quite different. The difference is due to the iron flux density value adopted in the analytic formula (6). It is fixed for the analytical model ($\hat{B}_t = 1.8$ T and $\hat{B}_{bi} = 1.6$ T), while from FE simulations such saturation values are quite different.

In both Fig. 7b and Fig. 7c, the working point of the motor tested is identified. It is characterized by a PM length of 12 mm and a diameter ratio equal to 0.58. From the torque map it can be deduced that by increasing the diameter ratio the magnet size could be reduced. Thus, the delivered torque does not change and the utilization of magnetic material is limited. However, it is observed from the Joule losses map that the operating point has relatively low losses. Therefore, in order to analyse the tested case, it is necessary to calculate the efficiency and compare it with the delivered torque.

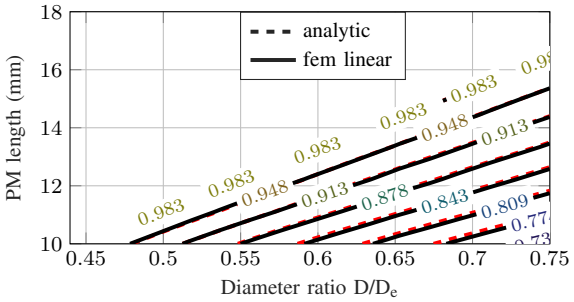

(a) Peak of the quasi-squared waveform.

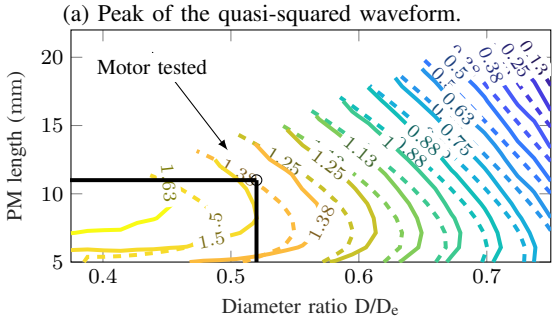

(b) Torque map.

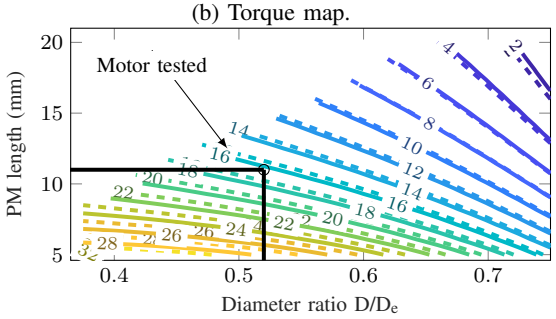

(c) Total losses map.

Fig. 7. Analytic (dashed lines) and FE (solid lines) results in the $D_i/D_e - h_m$ plane.

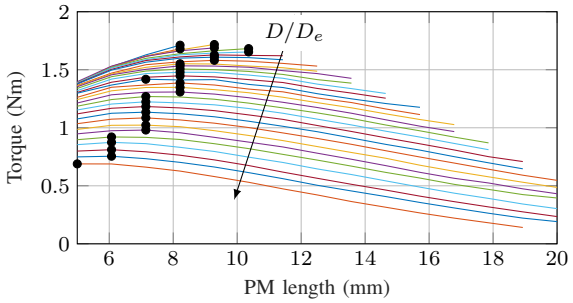

Fig. 8. Torque versus D with different h_m, FE simulation results.

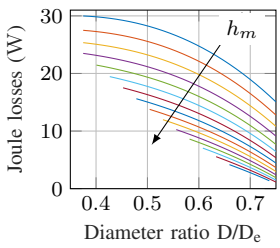

(a) Joule losses vs D/D_e.

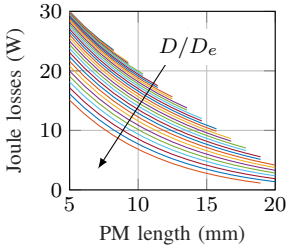

(b) Joule losses vs t_m.

Fig. 9. Losses versus D, with different h_m.

Fig. 8 shows the torque versus the PM length, considering different diameter ratios. Only FE simulation results are presented, since the comparison with the analytic results has already been shown. For a specific torque value, the optimal diameter and PM length combination can be identified.

Fig. 9a shows Joule losses variation with the stator inner diameter, considering different PM height values. They decrease as D increases, since copper volume is lower when stator slots become smaller. At the same time, fixing D value, Joule losses decrease as h_m increases, since the slot cross-section area slightly decreases. In fact, fixing the diameter value, the air gap flux density increases as the PM length increases. Consequently, the tooth width and the back-iron height increase to avoid saturation of the stator core. This leads to a slight decrease of the slot area, to compensate the higher magnetizing flux. A lower slot area yields a lower copper volume, thus lower Joule losses.

Iron losses decrease as D increases, as the total iron volume is reduced. When h_m increases, iron losses increase as saturation phenomena occur. Therefore, the dependence of iron losses on inner diameter and PM length is opposite to the variation of Joule losses. Consequently, the overall efficiency will mainly depend on the power delivered.

Fig. 10 shows both analytic and FE torque map together with efficiency map. It is worth noticing that the efficiency has a shape similar to the torque, as just commented. For a specific torque, the optimal diameter ratio and PM length can be identified by the point of intersection between the torque curve and the efficiency curve tangent to it. Such map allows to identify machine limits.

Considering the design of the commercial motor tested (i. e. 12 mm PM length, 0.58 diameter ratio), its position in the torque and efficiency map from simulation is non optimal. From FE simulations the torque is 1.25 N m, the power delivered is 393.3 W, and with total losses of 50.6 W the efficiency is 88.7 %. These results are quite similar to experimental measures. In the torque and efficiency map such motor configuration stays in a high-efficiency region. According to the map its design can be further improved maintaining the capabilities. Shifting the working point to the position of the blue filled point of Fig. 10b, the rated torque is equal to 1.25 N m as well, but the PM length is reduced to the value 7.5 mm, increasing the diameter ratio to 0.62. Such geometry yields an efficiency of 89.8 %.

VII. Conclusions

In this work, a 12 slots/10 poles motor is considered, first with an SPM and then with an IPM rotor geometry. The analysis takes into account both state-of-the-art constraints and variables that are manipulated through a preliminary analytical model and a subsequent finite element analysis simulation.

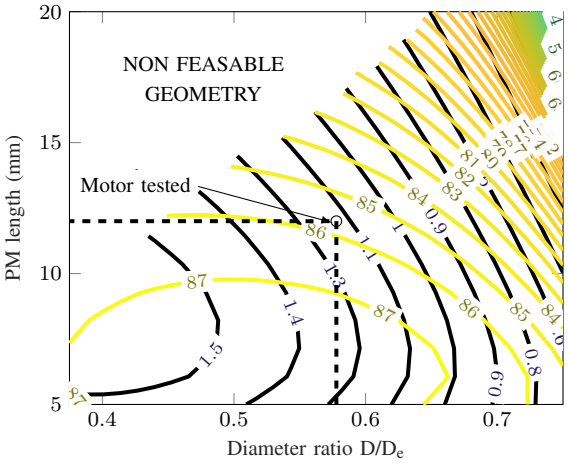

(a) Analytic.

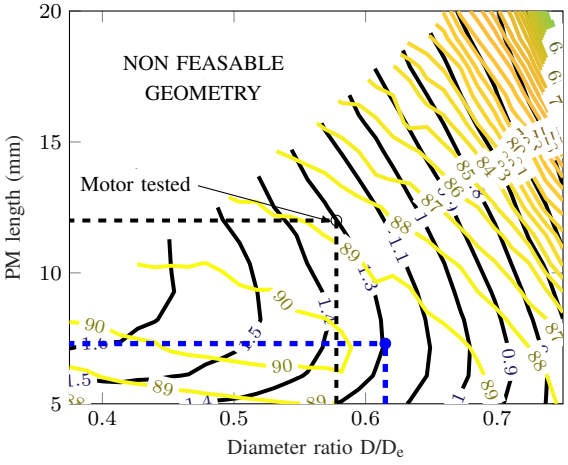

(b) FE.

Fig. 10. Torque (black lines) and efficiency (red lines) map varying D and h_m.

Both thermal and mechanical experimental tests are carried out for a commercial IPM motor, to define the typical requirements of electric motors for e-bike application. The goal is to find an optimal design that respects the constraints on motor size and improves the motor capabilities (torque density, efficiency).

The IPM motor design variables considered are the ratio between inner and outer stator diameters, and the PM length. Each variable combination leads to a motor model that has been analysed through FE simulation. Both the torque delivered and power losses are computed and a feasible design region defined. Is has been shown that an optimal design can be carried out choosing the best combination of diameter ratio and PM length. In particular, considering a specific torque value, the PM length can be reduced increasing the diameter ratio. Thus, the magnet material quantity decreases, while the motor efficiency slightly increases. If the inner diameter is reduced, both the torque delivered and the motor efficiency are higher.

REFERENCES

[1] W. C. Morchin and H. Oman, *Electric bicycles: a guide to design and use*. Electric Bicycle Manual, 2006, vol. 8.

[2] (2021) Projections for the global electric bike market between 2018 and 2028. [Online]. Available: https://www.statista.com/statistics/1261084/global-e-bike-market-forecast/

[3] A. Vagati, G. Franceschini, I. Marongiu, and G. P. Troglia, "Design criteria of high performance synchronous reluctance motors," in *Conf. Rec. IEEE-IAS Annu. Meeting*, vol. 1, 1992, pp. 66–73.

[4] A. Muetze and Y. C. Tan, "Electric bicycles - a performance evaluation," *IEEE Industry Applications Magazine*, vol. 13, no. 4, pp. 12–21, 2007.

[5] ——, "Modeling and analysis of the technical performance of DC-motor electric bicycle drives based on bicycle road test data," in *2007 IEEE International Electric Machines Drives Conference (IEMDC)*, vol. 2, 2007, pp. 1574–1581.

[6] E. Starschich and A. Muetze, "Comparison of the performances of different geared brushless-DC motor drives for electric bicycles," in *2007 IEEE International Electric Machines Drives Conference (IEMDC)*, vol. 1, 2007, pp. 140–147.

[7] K. F. I. Faruque, N. Nawshin, M. F. Bhuiyan, M. R. Uddin, M. Hasan, and K. M. Salim, "Design and development of bldc controller and its implementation on e-bike," in *2018 International Conference on Recent Innovations in Electrical, Electronics and Communication Engineering (ICRIEECE)*, 2018, pp. 1461–1465.

[8] S. K. Chawrasia, A. Das, and C. Kumar Chanda, "Design and analysis of electric bike hub-motor using motor-cad," in *2020 3rd International Conference on Energy, Power and Environment: Towards Clean Energy Technologies*, 2021, pp. 1–6.

[9] R. Nasiri-Zarandi, A. Karami-Shahnani, M. S. Toulabi, and A. Tessarolo, "Design and experimental performance assessment of an outer rotor pm-assisted synrm for the electric bike propulsion," *IEEE Transactions on Transportation Electrification*, vol. 9, no. 1, pp. 727–736, 2023.

[10] S. Koyuncu, U. Tuncer, A. Dalcali, and S. Oncu, "External rotor 6/8 switched reluctance motor design for e-bike," in *2021 10th International Conference on Renewable Energy Research and Application (ICRERA)*, 2021, pp. 131–135.

[11] B. Howey, B. Bilgin, and A. Emadi, "Design of an external-rotor direct drive e-bike switched reluctance motor," *IEEE Transactions on Vehicular Technology*, vol. 69, no. 3, pp. 2552–2562, 2020.

[12] A. M. EL-Refaie, "Fractional-slot concentrated-windings synchronous permanent magnet machines: Opportunities and challenges," *IEEE Transactions on Industrial Electronics*, vol. 57, no. 1, pp. 107–121, 2010.

[13] S.-o. Kwon, S.-i. Kim, P. Zhang, and J.-p. Hong, "Performance comparison of ipmsm with distributed and concentrated windings," in *Conference Record of the 2006 IEEE Industry Applications Conference Forty-First IAS Annual Meeting*, vol. 4, 2006, pp. 1984–1988.

[14] A. Di Gerlando, R. Perini, and M. Ubaldini, "High pole number, pm synchronous motor with concentrated coil armature windings," in *Recent Developments of Electrical Drives*. Springer, 2006, pp. 307–320.

[15] D. Meeker, "Finite element method magnetics (femm), version 4.2," *Web Page: http://femm. berlios. de*, 2006.